

A hybrid kinetic WGVC–WENO scheme for compressible flows

Kang He ^{a,b}, Hongwei Liu ^{a,*}, Xinliang Li ^{a,b}

^a State Key Laboratory of High Temperature Gas Dynamics, Institute of Mechanics, Chinese Academy of Sciences, Beijing 100190, China

^b School of Engineering Science, University of Chinese Academy of Sciences, Beijing 100049, China

ARTICLE INFO

Keywords:

Gas kinetic theory
WGVC–WENO methods
Hybrid flux
Numerical dissipation

ABSTRACT

In this paper, we propose a hybrid kinetic weighted group velocity control–weighted essentially non-oscillatory (WGVC–WENO) scheme which combines the WGVC–WENO reconstruction technique He et al. (2014) with the hybrid kinetic method proposed in Liu et al. (2015). The new scheme is based on the idea of hybridization. The hybrid kinetic method is adopted for flux calculations, and the WGVC–WENO technique is adopted for physical reconstructions. In smooth flow regions, the collision-related flux method and WGVC reconstruction technique play a leading role. The kinetic flux vector splitting (KFVS) method and WENO reconstruction technique are dominant in discontinuous regions. The third-order TVD Runge–Kutta method is used for temporal discretization. Many one-dimensional and two-dimensional numerical examples show that the new scheme has the properties of high accuracy, low dissipation, and good shock-capturing ability.

1. Introduction

Numerical simulations of turbulence and aeroacoustics require high-order methods for capturing more details such as turbulence structures and acoustic waves. In past decades, many high-order methods have been proposed, e.g., essentially non-oscillatory (ENO) schemes [1], weighted-ENO (WENO) schemes [2–8], monotonicity-preserving (MP) schemes [9,10], compact schemes [11,12], discontinuous Galerkin (DG) methods [13,14], and many others. Basically, high-order numerical methods consist of two main steps: physical reconstructions and flux calculations. For physical reconstructions, WENO schemes are widely used for solving hyperbolic conservation laws due to the strong robustness property and good shock-capturing ability. Liu et al. [2] originally proposed the WENO method based on the ENO [1] idea, then Jiang and Shu [3] improved it and constructed the WENO-JS scheme, which established the general framework of subsequent WENO schemes. Later, Henrick et al. [4] pointed out that the WENO-JS scheme cannot satisfy the fifth-order convergence conditions and proposed the WENO-M scheme, which improved the accuracy near the critical points. Borges et al. [5] also covered the convergence problem of the WENO-JS scheme by changing the smoothness indicator. Martin et al. [6] presented two symmetric WENO schemes with the bandwidth optimization for simulations of compressible turbulence. Shen and Zha [7] developed the multi-step WENO scheme to improve the accuracy in transitional points. Hong et al. [8] proposed the pre-discrete mapping method based on the WENO-M scheme to improve the computational efficiency. For flux calculations, there are mainly two kinds of approaches: flux

difference splitting (FDS) methods [15–17], flux vector splitting (FVS) methods [3,18,19], to name just a few. Usually, FDS methods have low dissipations, but sometimes they are less robust. FVS methods are highly robust and easy to construct, but their numerical dissipations are usually large, like the kinetic flux vector splitting approach [20].

Compared with traditional high-order methods based on Navier–Stokes equations, gas-kinetic schemes (GKS) [21–23] based on the Boltzmann equation have attracted much attention due to the consideration of the physical procedure of gas molecule movement and interaction. Some upwind methods based on the Boltzmann equation were developed in the early stage, such as the kinetic numerical method (KNM) [24] and kinetic flux vector splitting (KFVS) method [20,25–27]. Similar to FVS schemes, KFVS methods are highly robust. However, these methods ignore the collisional effects of gas molecules. Hence the numerical dissipation is large. After taking the collisional effects between gas molecules as well as coupling the inviscid and viscous fluxes, GKS methods can effectively calculate more complex flows, especially for hypersonic viscous flows [21–23]. The high-order GKS methods which improve the numerical accuracy while retaining the advantages of GKS framework have also been developed, for example, the high-order gas-kinetic scheme proposed by Li et al. [28], the high-order multidimensional gas-kinetic scheme proposed by Luo et al. [29], the two-stage fourth-order gas-kinetic scheme proposed by Pan et al. [30–32], the compact fourth-order gas-kinetic scheme on structured mesh, and unstructured mesh proposed by Ji et al. [33,34], the acoustic and shock wave capturing compact high-order gas-kinetic scheme proposed

* Corresponding author.

E-mail addresses: hekang@imech.ac.cn (K. He), hliu@imech.ac.cn (H. Liu), lixl@imech.ac.cn (X. Li).

by Zhao et al. [35], the arbitrary-Lagrangian–Eulerian high-order gas-kinetic scheme and fourth-order gas-kinetic scheme proposed by Pan et al. [36,37]. After years of development, GKS schemes have been gradually matured and extended to many application fields [38–40].

One of the research hotspots of high-order methods is hybrid schemes [41–46], such as the minimized dispersion and controllable dissipation (MDCD)-WENO scheme [44] and weighted group velocity control (WGVC)-WENO scheme [45], and many others. Hybrid schemes have the characteristics of using reconstruction methods with different dissipation in different regions. Before using reconstruction methods, it is necessary to adopt the shock detection methods [47–49] to determine whether the computational domain is smooth or not. Then, low dissipation schemes such as compact schemes can be used in smooth regions, and high dissipation schemes for example WENO methods can be adopted in discontinuous regions. In [50], Liu proposed a hybrid kinetic method that uses different kinetic flux methods in different regions. The less dissipative collision-related flux is used in smooth regions, and the more dissipative KFVS flux is adopted in discontinuous regions. Many numerical examples have validated the effectiveness of this method. Based on the essential idea of the hybrid kinetic flux, in this paper, a hybrid kinetic WGVC–WENO scheme is proposed, which combines the WGVC–WENO reconstruction method proposed by [45] with the hybrid kinetic method of [50]. Compared with [50], the new scheme has less dissipation while maintaining strong robustness and shock-capturing ability.

The structure of this paper is as follows: In Section 2, we first introduce the gas kinetic theory and WGVC–WENO reconstruction technique, then we describe how to combine the WGVC–WENO reconstruction technique with the hybrid kinetic method. In Section 3, several numerical examples are presented to validate the performance of our method. Finally, the conclusion is given in Section 4.

2. Hybrid kinetic WGVC–WENO scheme

In this section, we will present the hybrid kinetic WGVC–WENO scheme for solving the Euler equations. As a matter of convenience, only the one-dimensional form is presented, and it can be easily extended to multidimensional forms in a dimension by dimension manner [3].

The 1D Euler equations can be written as:

$$\frac{\partial \mathbf{U}}{\partial t} + \frac{\partial \mathbf{F}(\mathbf{U})}{\partial x} = 0. \quad (1)$$

where $\mathbf{U} = (\rho, \rho u, E)^T$, $\mathbf{F}(\mathbf{U}) = (\rho u, \rho u^2 + p, u(E + p))^T$, ρ is the fluid density, u is the velocity, p is the pressure, $E = \rho(e + u^2/2)$ is the total energy. For an ideal gas, the thermal energy e is related to the pressure p through the relation $p = (\gamma - 1)\rho e$, and here γ is the ratio of the specific heats.

For a uniform grid with the grid size Δx , the conservative finite difference method can be written as:

$$\frac{d\mathbf{U}_i}{dt} = -\frac{1}{\Delta x} (\hat{\mathbf{F}}_{i+1/2} - \hat{\mathbf{F}}_{i-1/2}). \quad (2)$$

where \mathbf{U}_i is the point value, and $\hat{\mathbf{F}}_{i+1/2}$ is the numerical flux which has an approximation of the flux $\mathbf{F}(\mathbf{U})$ at the boundary $x_{i+1/2}$. The third-order TVD Runge–Kutta method [51] will be used to integrate in time. Therefore we only need to specify the construction of the numerical flux $\hat{\mathbf{F}}_{i+1/2}$ for a conservative finite difference method.

2.1. Hybrid kinetic method

In this subsection, we will briefly review the hybrid kinetic method [50] which is based on the gas kinetic theory.

The well-known Boltzmann equation can be written as:

$$\frac{\partial f}{\partial t} + \sum_{m=1}^d v_m \frac{\partial f}{\partial x_m} = J(f, f). \quad (3)$$

where d is the space dimension, $\mathbf{v} = (v_1, \dots, v_d)^T$ denotes the gas molecules velocity, J is related to the collision term. Eq. (3) has a solution in the equilibrium state, that is, Maxwell equilibrium distribution function, which can be written as:

$$g(\mathbf{x}, t, \mathbf{v}, \xi) = \rho \left(\frac{\lambda}{\pi} \right)^{\frac{K+d}{2}} e^{-\lambda((\mathbf{v}-\mathbf{u})^2 + \xi^2)}. \quad (4)$$

where K is the total number of degrees of freedom for the internal degree of freedom variable ξ , $\xi^2 = \sum_{n=1}^K \xi_n^2$, $\lambda = M/2k_B T$, here M denotes the molecule mass, k_B is the Boltzmann constant, and T is the temperature.

For KFVS methods, the collisional effects between gas molecules are ignored. Hence, we can modify Eq. (3) by replacing the distribution function f with the Maxwellian distribution function:

$$\frac{\partial g}{\partial t} + \sum_{m=1}^d v_m \frac{\partial g}{\partial x_m} = 0. \quad (5)$$

Macroscopic variables can be obtained by the following equation:

$$\mathbf{U} = \int_{\mathcal{R}^{K+d}} \psi f(\mathbf{x}, t, \mathbf{v}, \xi) d\mathbf{v} d\xi = \int_{\mathcal{R}^{K+d}} \psi g(\mathbf{x}, t, \mathbf{v}, \xi) d\mathbf{v} d\xi. \quad (6)$$

where ψ is the vector of moments defined as:

$$\psi = \left(1, v_1, \dots, v_d, \frac{1}{2} (\mathbf{v}^2 + \xi^2) \right)^T. \quad (7)$$

Besides, the Euler equations can be gained by taking ψ to Eq. (5):

$$\frac{\partial}{\partial t} \int_{\mathcal{R}^{K+d}} \psi g(\mathbf{x}, t, \mathbf{v}, \xi) d\mathbf{v} d\xi + \sum_{m=1}^d \frac{\partial}{\partial x_m} \int_{\mathcal{R}^{K+d}} v_m \psi g(\mathbf{x}, t, \mathbf{v}, \xi) d\mathbf{v} d\xi = 0. \quad (8)$$

As shown in [50], the numerical flux $\hat{\mathbf{F}}_{i+1/2}$ in Eq. (2) can be divided into two parts:

$$\hat{\mathbf{F}}_{i+1/2} = \hat{\mathbf{F}}_{i+1/2}^+ + \hat{\mathbf{F}}_{i+1/2}^-. \quad (9)$$

where $\hat{\mathbf{F}}_{i+1/2}^+$ denotes the flux along increasing x direction and $\hat{\mathbf{F}}_{i+1/2}^-$ denotes the flux along decreasing x direction. Let $\mathbf{F}_i(\mathbf{U}_i)$ be the numerical flux based on the point value \mathbf{U}_i , and we can split the numerical flux \mathbf{F}_i into two parts:

$$\mathbf{F}_i = \mathbf{F}_i^+ + \mathbf{F}_i^-. \quad (10)$$

There are many flux splitting approaches for achieving Eq. (10), such as the Steger–Warming [18] or Lax–Friedrichs [3] flux splitting method. For a kinetic scheme, \mathbf{F}_i^\pm in Eq. (10) can be obtained from the KFVS method:

$$\mathbf{F}_i^+ = \int_{\mathcal{R}^K} \int_{\mathbf{v} > 0} \mathbf{v} \psi g(\mathbf{U}_i, \mathbf{v}, \xi) d\mathbf{v} d\xi, \quad \mathbf{F}_i^- = \int_{\mathcal{R}^K} \int_{\mathbf{v} < 0} \mathbf{v} \psi g(\mathbf{U}_i, \mathbf{v}, \xi) d\mathbf{v} d\xi. \quad (11)$$

It is noteworthy that we still need reconstruction techniques such as WENO schemes to reconstruct \mathbf{F}_i^\pm to obtain $\hat{\mathbf{F}}_{i+1/2}^\pm$ in Eq. (9).

Since it is well known that the numerical dissipations of the collisionless FVS/KFVS methods are intrinsically very large, in Ref [50], a hybrid kinetic WENO method was proposed to reduce the numerical dissipation in the flux evaluation procedure, which includes effects of both the free transfer and the collision of gas molecules.

The hybrid kinetic flux can be written as:

$$\hat{\mathbf{F}}_{i+1/2} = \alpha \hat{\mathbf{F}}_{i+1/2}^{\text{KFVS}} + (1 - \alpha) \hat{\mathbf{F}}_{i+1/2}^{\text{C}}. \quad (12)$$

where $\hat{\mathbf{F}}_{i+1/2}^{\text{KFVS}}$ is the collisionless KFVS-type numerical flux, $\hat{\mathbf{F}}_{i+1/2}^{\text{C}}$ is the numerical flux which considers collisional effects between gas molecules, and α is a weight parameter which should approach one around strong shock waves and zero in smooth regions to get a dissipation-adaptive numerical flux. More details about α will be given in Section 2.3.

In Eq. (12), the collisionless flux $\hat{\mathbf{F}}_{i+1/2}^{\text{KFVS}}$ can be obtained by the approach described in the preceding part, i.e., Eqs. (9)–(11). Next, we present constructions of the collision-related kinetic flux $\hat{\mathbf{F}}_{i+1/2}^{\text{C}}$.

Table 1The values of b_l .

$b_{-3}(\sigma_t)$	$b_{-2}(\sigma_t)$	$b_{-1}(\sigma_t)$	$b_0(\sigma_t)$	$b_1(\sigma_t)$	$b_2(\sigma_t)$	$b_3(\sigma_t)$
$-\sigma_t$	$1/60 + 6\sigma_t$	$37/60 + 20\sigma_t$	$-2/15 - 15\sigma_t$	$37/60 - 15\sigma_t$	$-2/15 + 6\sigma_t$	$1/60 - \sigma_t$

The basic idea of evaluating $\hat{\mathbf{F}}_{i+1/2}^C$ is to calculate the flux from $\mathbf{F}(\mathbf{U}) = (\rho u, \rho u^2 + p, u(E + p))^T$ based on the collision-related state $\hat{\mathbf{U}}_{i+1/2}^C$ constructed at the boundary $x_{i+1/2}$. To get $\hat{\mathbf{U}}_{i+1/2}^C$, we first split the conservative variable \mathbf{U}_i into two parts:

$$\mathbf{U}_i = \mathbf{U}_i^+ + \mathbf{U}_i^- \quad (13)$$

With

$$\mathbf{U}_i^+ = \int_{R^K} \int_{v>0} \psi \mathbf{g}(\mathbf{U}_i, \mathbf{v}, \xi) d\mathbf{v} d\xi, \quad \mathbf{U}_i^- = \int_{R^K} \int_{v<0} \psi \mathbf{g}(\mathbf{U}_i, \mathbf{v}, \xi) d\mathbf{v} d\xi. \quad (14)$$

Then the collision-related state $\hat{\mathbf{U}}_{i+1/2}^C$ can be obtained by:

$$\hat{\mathbf{U}}_{i+1/2}^C = \hat{\mathbf{U}}_{i+1/2}^+ + \hat{\mathbf{U}}_{i+1/2}^- \quad (15)$$

where $\hat{\mathbf{U}}_{i+1/2}^+$ is calculated from \mathbf{U}_i^+ by the reconstruction techniques such as WENO schemes, and $\hat{\mathbf{U}}_{i+1/2}^-$ is determined from \mathbf{U}_i^- by a symmetric procedure with respect to $x_{i+1/2}$. After $\hat{\mathbf{U}}_{i+1/2}^C$ is determined, from which the collision-related numerical flux $\hat{\mathbf{F}}_{i+1/2}^C$ can be evaluated.

2.2. WGVC–WENO reconstruction technique

In [45], He et al. first proposed the WGVC scheme and then combined it with the WENO scheme to get the WGVC–WENO method. Different from the classical Dispersion-Relation-Preserving(DRP) technique, the WGVC–WENO method is a nonlinear optimization technique, which has very good dispersion as well as attractive dissipation. In addition to the good spectral properties, the implementation of this method is also very simple. More details about the WGVC–WENO method are as follows:

To begin with, we assume $\hat{f}_{i+1/2}$ is the flux reconstructed from f_i that ranges over mesh point indices $i - (r - 1)$ to $i + (r - 1)$, here $r = 4$ for the seventh-order WGVC scheme. $\hat{f}_{i+1/2}$ is weighted by a mixed type flux [52] $\hat{f}_{i+1/2}(\sigma_m)$ and a slow type flux [52] $\hat{f}_{i+1/2}(\sigma_s)$:

$$\hat{f}_{i+1/2} = \varpi_m \hat{f}_{i+1/2}(\sigma_m) + \varpi_s \hat{f}_{i+1/2}(\sigma_s), \quad (16)$$

$$\hat{f}_{i+1/2}(\sigma_t) = \sum_{l=-(r-1)}^{r-1} b_l(\sigma_t) \cdot f_{i+l}, \quad t = m, s. \quad (17)$$

where $t = m$ denotes the mixed type and $t = s$ denotes the slow type. σ_t is a free parameter for adjusting the dispersion characteristics of the fluxes. More details about σ_t can be found in [45]. In this paper, $\sigma_m = 0.02205$ and $\sigma_s = 0$. The values of b_l are listed in Table 1.

In Eq. (16), ϖ_m is the weight for the mixed type flux and ϖ_s is the weight for the slow type flux. The computational domain should be divided into two sub-stencil: S_m ranges over mesh point indices $i - (r - 1)$ to i and S_s ranges over mesh point indices i to $i + (r - 1)$. ϖ_m, ϖ_s are defined similar to the weights for WENO-Z scheme [5], that is:

$$\gamma_t = D_t \left[1 + \left(\frac{\tau}{\beta_t + \epsilon} \right)^p \right], \quad t = m, s, \quad (18)$$

$$\varpi_t = \frac{\gamma_t}{\gamma_m + \gamma_s}. \quad (19)$$

With:

$$\beta_t = f_t'^2 + \frac{13}{12} f_t''^2 + \frac{1043}{960} f_t'''^2 + \frac{1}{12} f_t' f_t''', \quad t = m, s, \quad (20)$$

$$\tau = |\beta_m - \beta_s|. \quad (21)$$

Table 2The values of g_l .

g_0	g_1	g_2	g_3
0.0882	$1/5 + 0.441\varpi_m$	$3/5 - 0.2646\varpi_m$	$1/5 - 0.2646\varpi_m$

In Eq. (18), ϵ is a small positive number to prevent division by zero, here $\epsilon = 10^{-40}$ and $p = 2$ as [5]. D_m, D_s are optimal weights that can combine the mixed type flux $\hat{f}_{i+1/2}(\sigma_m)$ and the slow type flux $\hat{f}_{i+1/2}(\sigma_s)$ into a seventh-order upwind flux in smooth regions, here $D_m = 0.32394$ and $D_s = 0.67606$.

In order to combine the WGVC scheme with WENO scheme, [45] rewrote the WGVC scheme based on candidate stencils for the WENO scheme, as follows:

$$\hat{f}_{i+1/2} = \sum_{l=0}^{r-1} g_l \hat{f}_{i+1/2,l}, \quad (22)$$

$$\begin{aligned} \hat{f}_{i+1/2,0} &= -\frac{3}{12} f_{i-3} + \frac{13}{12} f_{i-2} - \frac{23}{12} f_{i-1} + \frac{25}{12} f_i, \\ \hat{f}_{i+1/2,1} &= \frac{1}{12} f_{i-2} - \frac{5}{12} f_{i-1} + \frac{13}{12} f_i + \frac{3}{12} f_{i+1}, \\ \hat{f}_{i+1/2,2} &= -\frac{1}{12} f_{i-1} + \frac{7}{12} f_i + \frac{7}{12} f_{i+1} - \frac{1}{12} f_{i+2}, \\ \hat{f}_{i+1/2,3} &= \frac{3}{12} f_i + \frac{13}{12} f_{i+1} - \frac{5}{12} f_{i+2} + \frac{1}{12} f_{i+3}. \end{aligned} \quad (23)$$

The values of g_l are listed in Table 2. Based on Eq. (22), It is convenient to combine the WGVC scheme with WENO scheme:

$$\hat{f}_{i+1/2} = \sum_{l=0}^{r-1} \omega_l^{\text{hybrid}} \hat{f}_{i+1/2,l}, \quad (24)$$

$$\omega_l^{\text{hybrid}} = (1 - \theta) g_l + \theta \omega_l. \quad (25)$$

where $(1 - \theta) g_l$ is the new weight for the WGVC scheme and $\theta \omega_l$ is the new weight for the WENO-Z scheme, here ω_l are defined similarly to Eqs. (18)–(21). θ is a parameter that meets the condition: $\theta(0) = 0$, $\theta(1) = 1$. Moreover, θ is defined as Eqs. (26)–(27):

$$\theta = s^q \cdot (q + 1 - q \cdot s), \quad (26)$$

$$s = 1 - \frac{\sigma_m \varpi_s}{D_m D_s}. \quad (27)$$

In Eq. (26), q is a positive integer. A large number of numerical experiments show that the dissipation decreases with the increase of q . In this paper, $q = 100$. So far, the basic idea of the WGVC–WENO reconstruction technique has been introduced.

2.3. Hybrid kinetic WGVC–WENO scheme

The strategy of the hybrid kinetic WGVC–WENO scheme is to adopt different flux methods and reconstruction techniques according to the different characteristics of the flow fields. Ideally, collision-related kinetic flux $\hat{\mathbf{F}}_{i+1/2}^C$ and the WGVC reconstruction technique should be used in smooth regions. Collisionless KFVS-type flux with the WENO-Z reconstruction technique should play a role in discontinuity regions.

Due to the limitation of the current shock detection methods, it is challenging to adopt a single flux method and reconstruction technique in compressible flows with strong shock waves. The compromise is to use weighted methods based on the smoothness evaluation of flows. In Eq. (12), the weight parameter α should be constructed by the principle that the contribution of the more dissipative flux $\hat{\mathbf{F}}_{i+1/2}^{\text{KFVS}}$ should be dominant around strong shock waves and small in smooth regions where the less dissipative flux $\hat{\mathbf{F}}_{i+1/2}^C$ should dominate. In the present study, we use the way of local pressure jump as [50]. By this means, the value of α in Eq. (12) can be determined by:

$$\alpha = 1 - \exp \left(-C \frac{|p_i - p_{i+1}|}{p_i + p_{i+1}} \right). \quad (28)$$

where p_i and p_{i+1} are pressures corresponding to values U_i and U_{i+1} , and C is a positive empirical constant that is set to be 10 in this paper. In order to improve the efficiency of the hybrid scheme, the following cut-off type of hybrid flux is used:

$$\hat{F}_{i+1/2} = \begin{cases} \hat{F}_{i+1/2}^C, & 0 \leq \alpha \leq \delta, \\ \alpha \hat{F}_{i+1/2}^{KFVS} + (1-\alpha) \hat{F}_{i+1/2}^C, & \delta < \alpha < 1-\delta, \\ \hat{F}_{i+1/2}^{KFVS}, & 1-\delta \leq \alpha \leq 1. \end{cases} \quad (29)$$

where δ is a parameter to control the cut-off range of α , which is set to be $\delta = 0.02$ in this paper. Using the cut-off type of hybrid flux, much computational cost can be saved without apparent accuracy debasement.

The construction procedure of the flux $\hat{F}_{i+1/2}$ when $\delta < \alpha < 1-\delta$ in Eq. (29) can be summarized as the follows:

1. Calculate the left and right eigenvector matrixes $L_{i+1/2}$ and $R_{i+1/2}$ by Roe average of variables \bar{U}_i and \bar{U}_{i+1} .
2. Calculate the jump indicator α by Eq. (29).
3. Calculate the variables F_{i+1}^\pm , U_{i+1}^\pm ($l = -3, \dots, 4$) defined by Eqs. (11) and (14), respectively.
4. Transform the variables F_{i+1}^\pm , U_{i+1}^\pm into the local characteristic fields as following:

$$\tilde{F}_i^\pm = L_{i+1/2} F_{i+1}^\pm, \quad \tilde{U}_i^\pm = L_{i+1/2} U_{i+1}^\pm. \quad (30)$$

5. Adopt the WGVC-WENO reconstruction technique for characteristic variables \tilde{F}_{i+1}^\pm and \tilde{U}_{i+1}^\pm to obtain the corresponding component of $\hat{F}_{i+1/2}^\pm$ and $\hat{U}_{i+1/2}^\pm$ at the boundary $x_{i+1/2}$.
6. Transform $\hat{F}_{i+1/2}^\pm$ and $\hat{U}_{i+1/2}^\pm$ back into the physical space and calculate the flux $\hat{F}_{i+1/2}^{KFVS}$ and $\hat{F}_{i+1/2}^C$ as follows:

$$\hat{F}_{i+1/2}^{KFVS} = R_{i+1/2} \left(\hat{F}_{i+1/2}^+ + \hat{F}_{i+1/2}^- \right), \quad (31)$$

$$\hat{U}_{i+1/2}^C = R_{i+1/2} \left(\hat{U}_{i+1/2}^+ + \hat{U}_{i+1/2}^- \right).$$

$$\hat{F}_{i+1/2}^C = F(\hat{U}_{i+1/2}^C). \quad (32)$$

7. Calculate hybrid numerical flux $\hat{F}_{i+1/2}$ by Eq. (32).

Besides, the construction procedures of the flux $\hat{F}_{i+1/2}$ when $0 \leq \alpha \leq \delta$ and $1-\delta \leq \alpha \leq 1$ can be easily obtained, which are omitted here.

2.4. Method for viscous terms

For viscous flows, the conventional sixth-order central difference scheme is used to discrete the viscous term. Take the two-dimensional case as an example, we have:

$$\left(\frac{\partial f}{\partial x} \right)_{i,j} = \frac{45(f_{i+1,j} - f_{i-1,j}) - 9(f_{i+2,j} - f_{i-2,j}) + (f_{i+3,j} - f_{i-3,j})}{60\Delta x}, \quad (33)$$

$$\left(\frac{\partial f}{\partial y} \right)_{i,j} = \frac{45(f_{i,j+1} - f_{i,j-1}) - 9(f_{i,j+2} - f_{i,j-2}) + (f_{i,j+3} - f_{i,j-3})}{60\Delta y}. \quad (34)$$

3. Numerical results and discussion

In this section, we will test the hybrid kinetic WGVC-WENO scheme in both one-dimensional and two-dimensional cases. A dimension by

Table 3

L_1 errors and convergence orders of WGVCW-HK, WGVCW-KFVS, WGVCW-SW for the 1D linear advection equation with initial condition (36) at $t = 2$ s.

N	WGVCW-HK		WGVCW-KFVS		WGVCW-SW	
	L_1	Order	L_1	Order	L_1	Order
8	8.780E-04	–	1.090E-03	–	2.008E-03	–
16	1.990E-05	5.46	3.120E-05	5.13	4.547E-05	5.46
32	2.060E-07	6.59	4.020E-07	6.28	5.614E-07	6.34
64	1.730E-09	6.90	3.500E-09	6.84	4.904E-09	6.84
128	1.390E-11	6.96	2.840E-11	6.95	3.948E-11	6.96

Table 4

L_1 errors and convergence orders of WGVCW-HK, WGVCW-KFVS, WGVCW-SW for the 2D linear advection equation with initial condition (38) at $t = 2$ s.

N^2	WGVCW-HK		WGVCW-KFVS		WGVCW-SW	
	L_1	Order	L_1	Order	L_1	Order
8^2	6.754E-04	–	1.940E-03	–	2.525E-03	–
16^2	1.466E-05	5.53	7.680E-05	4.66	9.872E-05	4.68
32^2	1.396E-07	6.71	8.982E-07	6.42	1.137E-06	6.44
64^2	1.154E-09	6.92	7.701E-09	6.87	9.708E-09	6.87
128^2	9.264E-12	6.96	6.147E-11	6.97	7.735E-11	6.97

dimension manner [3] has been used for the present finite difference method in two-dimensional cases. The uniform mesh is used for both 1D and 2D cases except for the laminar boundary layer problem. For the sake of simplicity, the WGVC-WENO reconstruction technique with the hybrid kinetic method will be called WGVCW-HK, the WENO reconstruction technique with the hybrid kinetic method will be called WENO-HK, the WENO reconstruction technique with the Steger-Warming method will be called WENO-SW, the WGVC-WENO reconstruction technique with the Steger-Warming method will be called WGVCW-SW, and the WGVC-WENO reconstruction technique with the KFVS method will be called WGVCW-KFVS. For all numerical examples, the computational time step Δt is:

$$\Delta t = \left| \frac{\eta \Delta_L}{(|u| + a)(1 + Re^*)} \right|_{\min}. \quad (35)$$

where the CFL number η is set to be 0.6. Δ_L is the representative length defined by $\Delta_L = \Delta x$ for 1D cases and $\Delta_L = \min\{\Delta x, \Delta y\}$ for 2D cases. a is the speed of sound defined by $a = \sqrt{\gamma p/\rho}$. Re^* is the grid Reynolds number defined by $Re^* = 0$ for inviscid flows and $Re^* = |u|\Delta_L/\nu$ for viscous flows, here ν is the kinematic viscosity coefficient.

3.1. Accuracy test

Both 1D and 2D examples are used to test the accuracy of the hybrid kinetic WGVCW-WENO scheme in this subsection. The 1D Euler equations with the following initial data are solved.

$$p(x, 0) = 1 + 0.2 \sin(\pi x), \quad u(x, 0) = 1.0, \quad p(x, 0) = 1. \quad (36)$$

The computational domain is $[0, 2]$, and the periodic boundary condition is used in this case. The exact solution for Eq. (36) is given by:

$$p(x, t) = 1 + 0.2 \sin(\pi(x - ut)), \quad u(x, t) = 1.0, \quad p(x, t) = 1. \quad (37)$$

The computational results with a suitably reduced time step when $t = 2$ s are shown in Table 3, where N is the grid points. It shows that three schemes can achieve a seventh-order convergence rate, and the WGVCW-HK has smaller absolute errors than the WGVCW-KFVS and WGVCW-SW for the same grid points. This means that WGVCW-HK is more accurate and less dissipative than other schemes.

Furthermore, the 2D Euler equations with the following initial data are solved.

$$p(x, y, 0) = 1 + 0.2 \sin(\pi(x + y)), \quad u_1 = 0.7, \quad u_2 = 0.3, \quad p = 1. \quad (38)$$

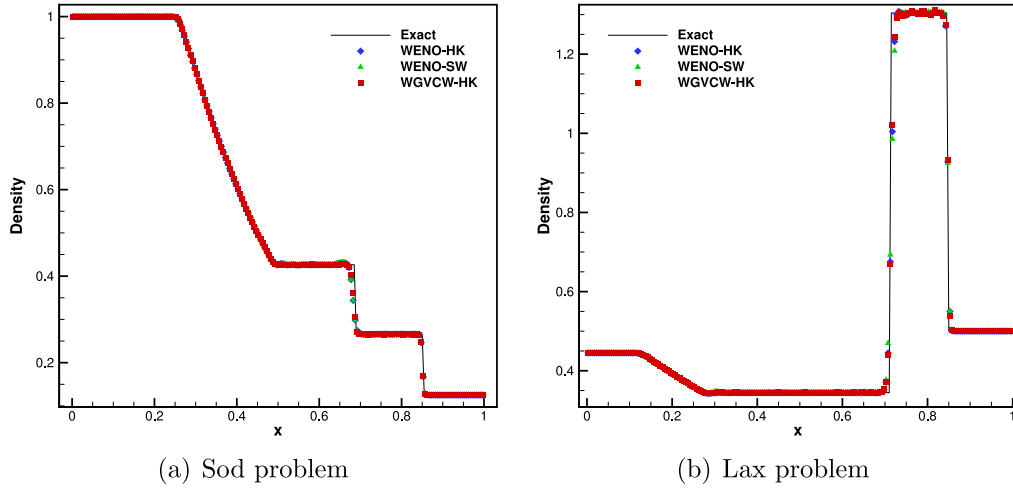


Fig. 1. Density profiles of the Sod problem (a) and Lax problem (b) with WGVCW-HK, WENO-HK, WENO-SW with 200 grid points.

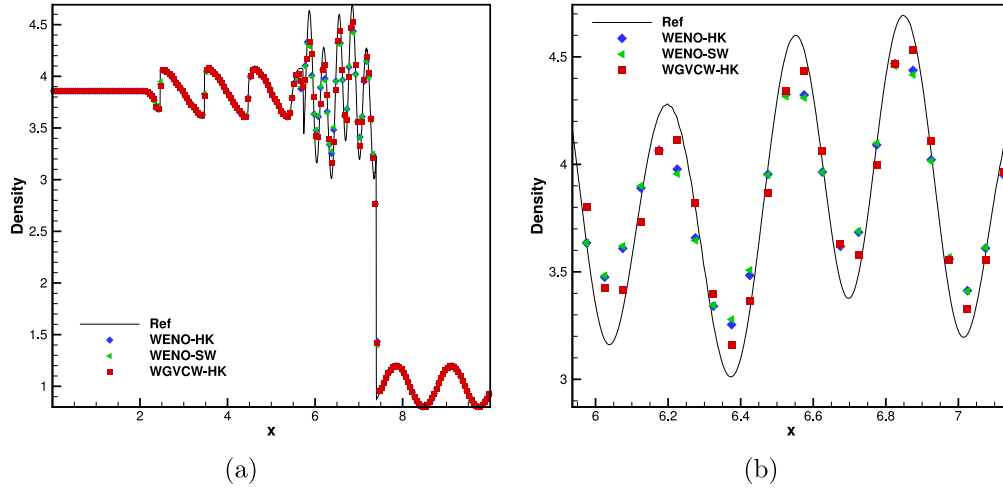


Fig. 2. Density profiles of Shu-Osher problem with WGVCW-HK, WENO-HK, WENO-SW at $t = 1.8$ s with 200 grid points (a) and an enlarged view (b).

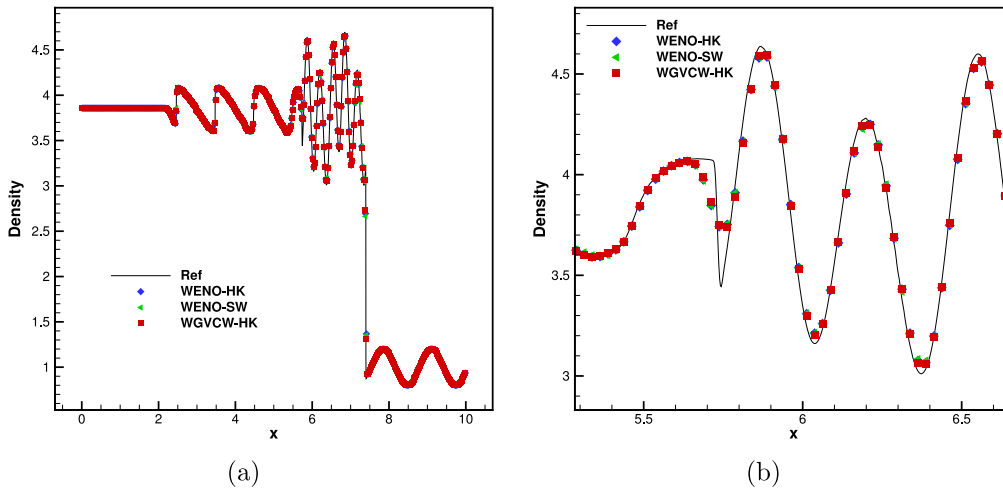


Fig. 3. Density profiles of Shu-Osher problem with WGVCW-HK, WENO-HK, WENO-SW at $t = 1.8$ s with 400 grid points (a) and an enlarged view (b).

The computational domain is taken as $[0,2] \times [0,2]$, the computational time is 2 s, and the periodic boundary condition is used along with each direction. The exact solution for this test is given by:

$$\rho(x, y, t) = 1 + 0.2 \sin(\pi(x + y - t)), \quad u_1 = 0.7, \quad u_2 = 0.3, \quad p = 1. \quad (39)$$

The errors and convergence orders of density ρ are shown in Table 4. Like 1D accuracy test results, the WGVCW-HK is more accurate and less dissipative than other schemes in the 2D test. Besides, the advantage

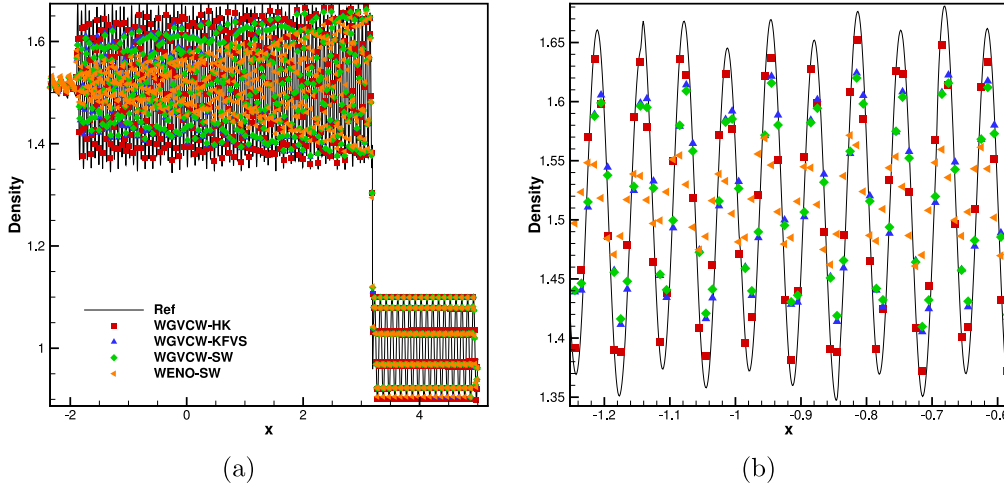


Fig. 4. Density profiles of Titarev-Toro problem with WGVCW-HK, WGVCW-KFVS, WGVCW-SW, WENO-SW at $t = 5$ s with 1000 grid points (a) and an enlarged view (b).

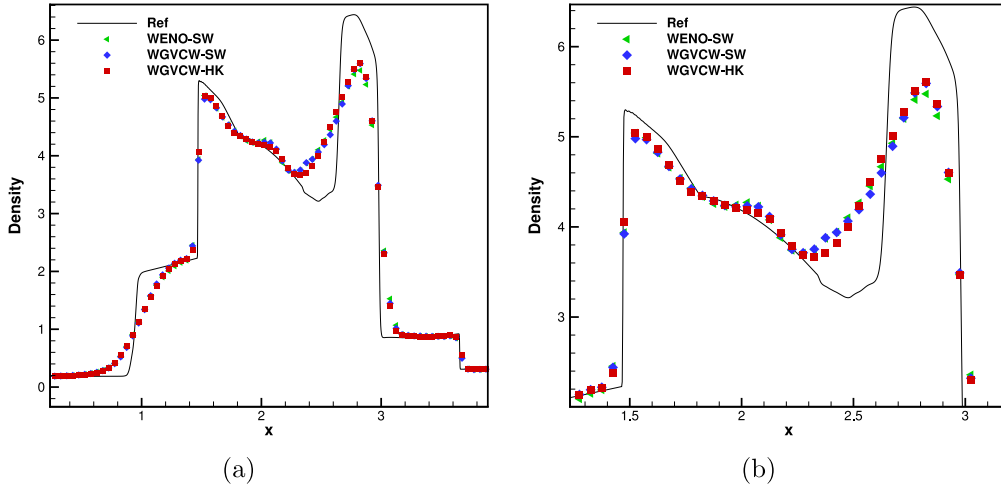


Fig. 5. Density profiles of blast wave problem with WGVCW-HK, WGVCW-SW, WENO-SW at $t = 0.38$ s with 200 grid points (a) and an enlarged view (b).

of WGVCW-HK in absolute error is more evident with the increase of dimension.

3.2. 1D Riemann problems

In this subsection, we consider the classical Riemann initial value problems, also known as the shock-tube problems: the Sod problem and Lax problem. These cases are solved by the WGVCW-HK, WENO-SW, and WENO-HK with 200 grid points.

For the Sod problem, the initial condition in the left and the right stages of the shock are:

$$(\rho, u, p) = \begin{cases} (1.000, & 0, & 1.0), & 0 \leq x < 0.5, \\ (0.125, & 0, & 0.1), & 0.5 \leq x \leq 1. \end{cases} \quad (40)$$

For the Lax problem, the initial condition in the left and the right stages of the shock are:

$$(\rho, u, p) = \begin{cases} (0.445, & 0.698, & 0.3528), & 0 \leq x < 0.5, \\ (0.500, & 0.000, & 0.5710), & 0.5 \leq x \leq 1. \end{cases} \quad (41)$$

The computational time for the Sod problem is $t = 0.2$ s and $t = 0.14$ s for the Lax problem, the computational domain is taken as $[0, 1]$ in both cases. As shown in Fig. 1, the simulated density ρ of the Sod and Lax problems indicate that the WGVCW-HK is slightly more accurate than the WENO-HK and WENO-SW due to its less dissipativity.

3.3. Shu-Osher problem

Shu-Osher problem is a one-dimensional case with a Mach 3 shock-entropy wave interaction, and it is mainly used to evaluate the resolution of the strong and the small waves [51]. The initial condition is as follow:

$$(\rho, u, p) = \begin{cases} (3.857143, 2.629369, 10.333333), & 0 \leq x \leq 1, \\ (1 + 0.2 \sin(5x), 0, 1), & 1 < x \leq 10. \end{cases} \quad (42)$$

The WGVCW-HK, WENO-SW, and WENO-HK are used for solving this problem with 200 and 400 grid points. The computational time is $t = 1.8$ s. Moreover, the numerical solution of the WGVCW-HK with $N = 4000$ is considered as the reference solution, whereas the analytic solution is non-existent. Fig. 2 shows that WGVCW-HK gives a much better result than WENO-HK and WENO-SW with the same grid points. In Fig. 3, the results of three methods are close, and the WGVCW-HK is slightly better than other methods.

3.4. Titarev-Toro problem

Titarev-Toro problem is based on the Shu-Osher problem, but it is more complicated due to the higher frequency entropy waves [53]. The initial condition is:

$$(\rho, u, p) = \begin{cases} (1.515695, 0.523346, 1.805), & -5 \leq x \leq -4.5, \\ (1 + 0.1 \sin(20\pi x), 0, 1), & -4.5 < x \leq 5. \end{cases} \quad (43)$$

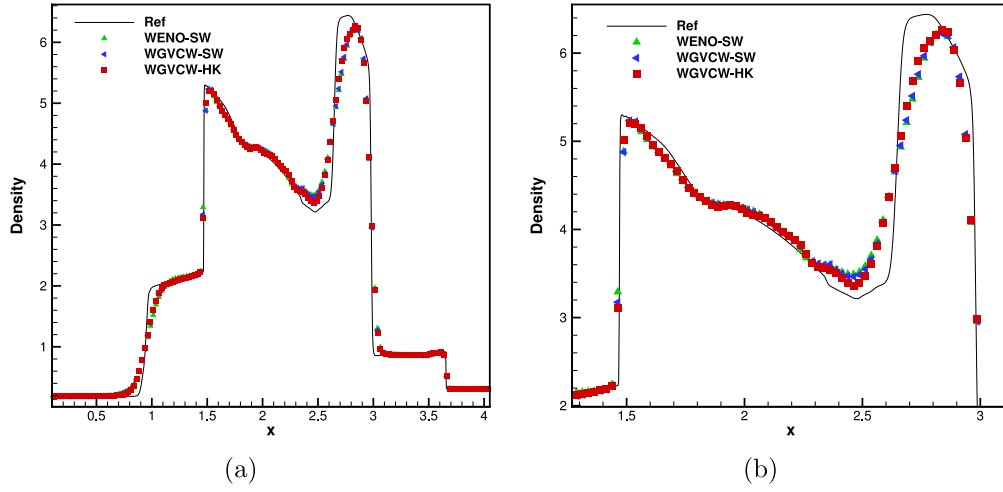


Fig. 6. Density profiles of blast wave problem with WGVCW-HK, WGVCW-SW, WENO-SW at $t = 0.38$ s with 400 grid points (a) and an enlarged view (b).

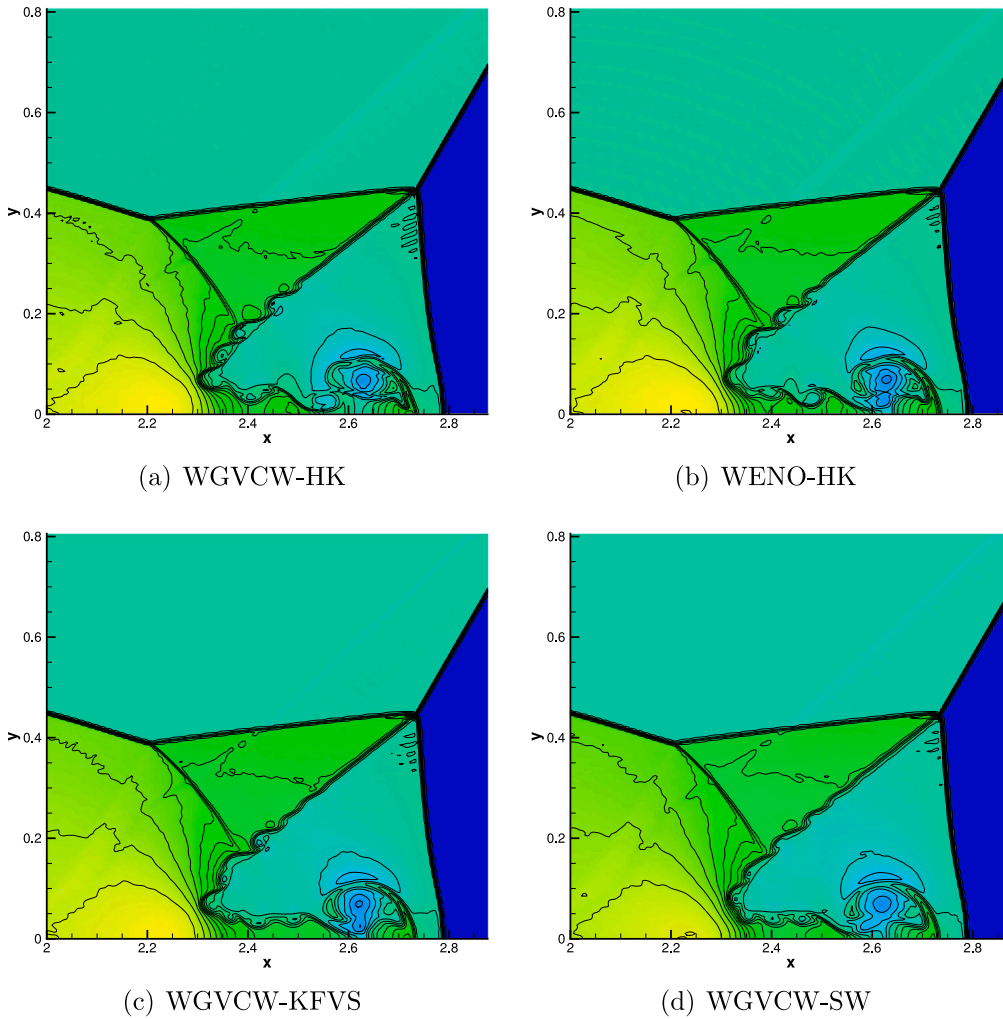


Fig. 7. Density profiles of double Mach reflection problem with WGVCW-HK (a), WENO-HK (b), WGVCW-KFVS (c), WGVCW-SW (d) at $t = 0.38$ s with 960×240 grid points; 30 equally spaced contour lines from $\rho = 1.5$ to $\rho = 22.9705$.

The WGVCW-HK, WGVCW-KFVS, WGVCW-SW, and WENO-SW are used for solving this problem with 800 grid points. The computational time is $t = 5.0$ s. Moreover, the numerical solution of the WGVCW-HK with $N = 8000$ is considered as the reference solution. The density profiles of the Titarev-Toro problem are shown in Fig. 4

that indicates the high-frequency waves decay after passing the shock wave. However, the numerical solution of WGVCW-HK is sharper than that of WGVCW-KFVS, WGVCW-SW, and WENO-SW at every peak, especially near the front shock wave. It means that WGVCW-HK is more sensitive to higher frequency waves, and WGVCW-HK shows better

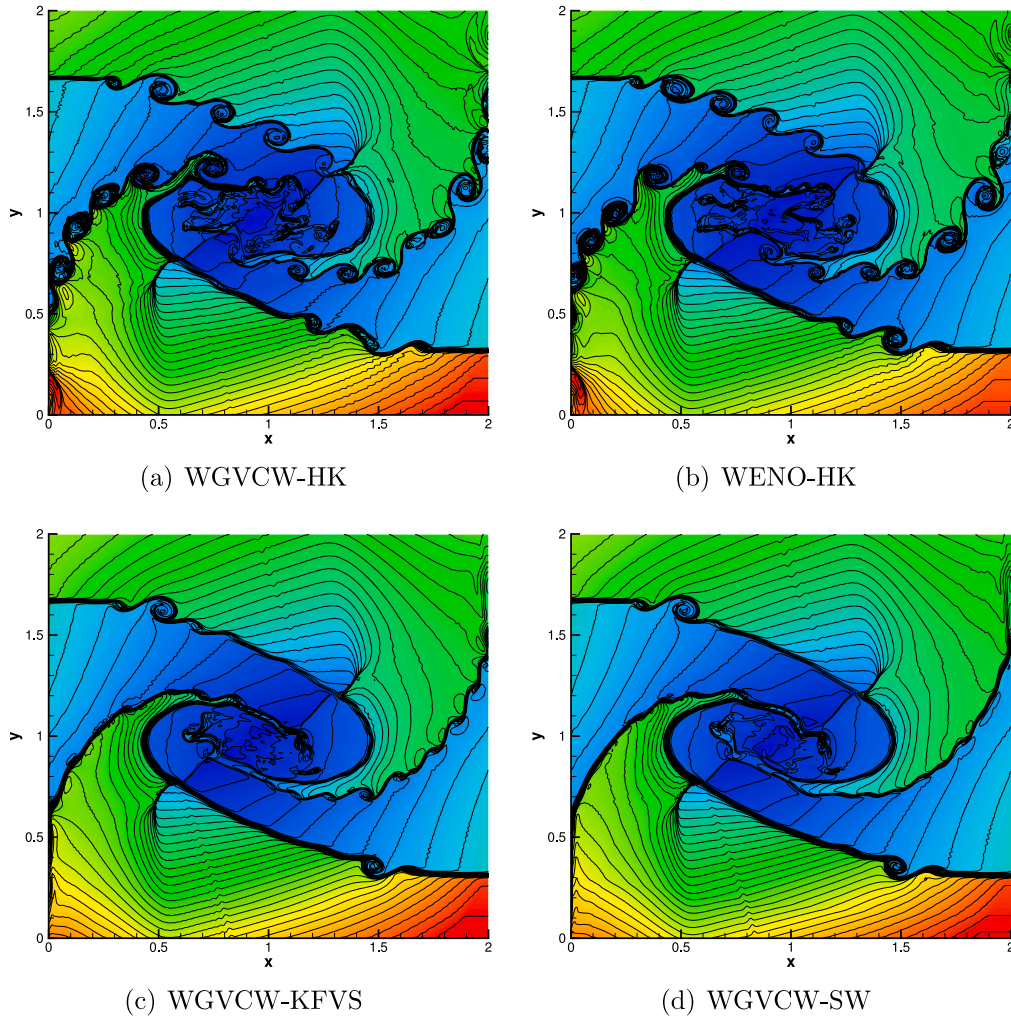


Fig. 8. Density profiles of 2D Riemann problem with WGVCW-HK (a), WENO-HK (b), WGVCW-KFVS (c), WGVCW-SW (d) at $t = 1.6$ s with 400×400 grid points; 50 equally spaced contour lines from $\rho = 0.1$ to $\rho = 3.2$.

discontinuity-capturing ability in the region with the rapidly changing waves. The performance of WGVCW-HK in this case is mainly due to the good spectral properties of the WGVC-WENO method, which is also mentioned by Liao et al. in [54].

3.5. Blast wave problem

In this case, the blast wave problem [5] is solved by the WGVCW-HK, WGVCW-SW, and WENO-SW with the initial flow field:

$$(\rho, u, p) = \begin{cases} (1, 0, 1000), & -5 \leq x < -4, \\ (1, 0, 0.01), & -4 \leq x < 4, \\ (1, 0, 100), & 4 \leq x \leq 5. \end{cases} \quad (44)$$

The computational domain is taken as $[-5, 5]$ with a reflecting boundary condition on both sides. The numerical results in $t = 0.38$ s with $N = 200$ are shown in Fig. 5, and $N = 400$ are shown in Fig. 6. Since there is no exact solution for this example, the WGVCW-SW with $N = 4000$ is used for comparison. As plotted in Figs. 5–6, WGVCW-HK obtains a better result than WGVCW-SW and WENO-SW especially in the turn region.

3.6. Double Mach reflection problem

The double-Mach reflection problem [55] is a two-dimensional case. There is a right-moving Mach 10 shock wave, positioned at $x = 1/6$, $y =$

0, and forms a 60 degree angle with increasing direction. The WGVCW-HK, WGVCW-KFVS, WGVCW-SW, and WENO-HK are applied to solve it. The parameters before the shock wave are $\rho = 1.4$, $p = 1$, $\gamma = 1.4$. For the bottom boundary, the exact post-shock solutions are used when $0 \leq x \leq 1/6$, and the reflecting boundary condition is used for other intervals. The upper boundary solutions are imposed to describe the exact motion of the Mach 10 shock wave. For the left and right boundary, the inflow and outflow boundary conditions are applied, respectively. The initial condition is:

$$(\rho, u_1, u_2, p) = \begin{cases} (8, 7.145, -4.125, 116.5), & y > \sqrt{3} \left(x - \frac{1}{6} \right), \\ (1.4, 0, 0, 1), & y \leq \sqrt{3} \left(x - \frac{1}{6} \right). \end{cases} \quad (45)$$

The computational domain is $[0, 4] \times [0, 1]$. The computational time is $t = 0.2$ s with 960×240 grid points. Since the Mach number is extremely high, the computation is straightforward to diverge if the scheme lacks sufficient robustness. It can be found that there are several flow characteristics around the Mach stems, slip lines, and incident shock from the density contours in Fig. 7. Compared with other schemes, WGVCW-HK captures better rolled-up small vortices and more complex shear surfaces along the incline Mach stems. It indicates that WGVCW-HK has smaller dissipation than other schemes.

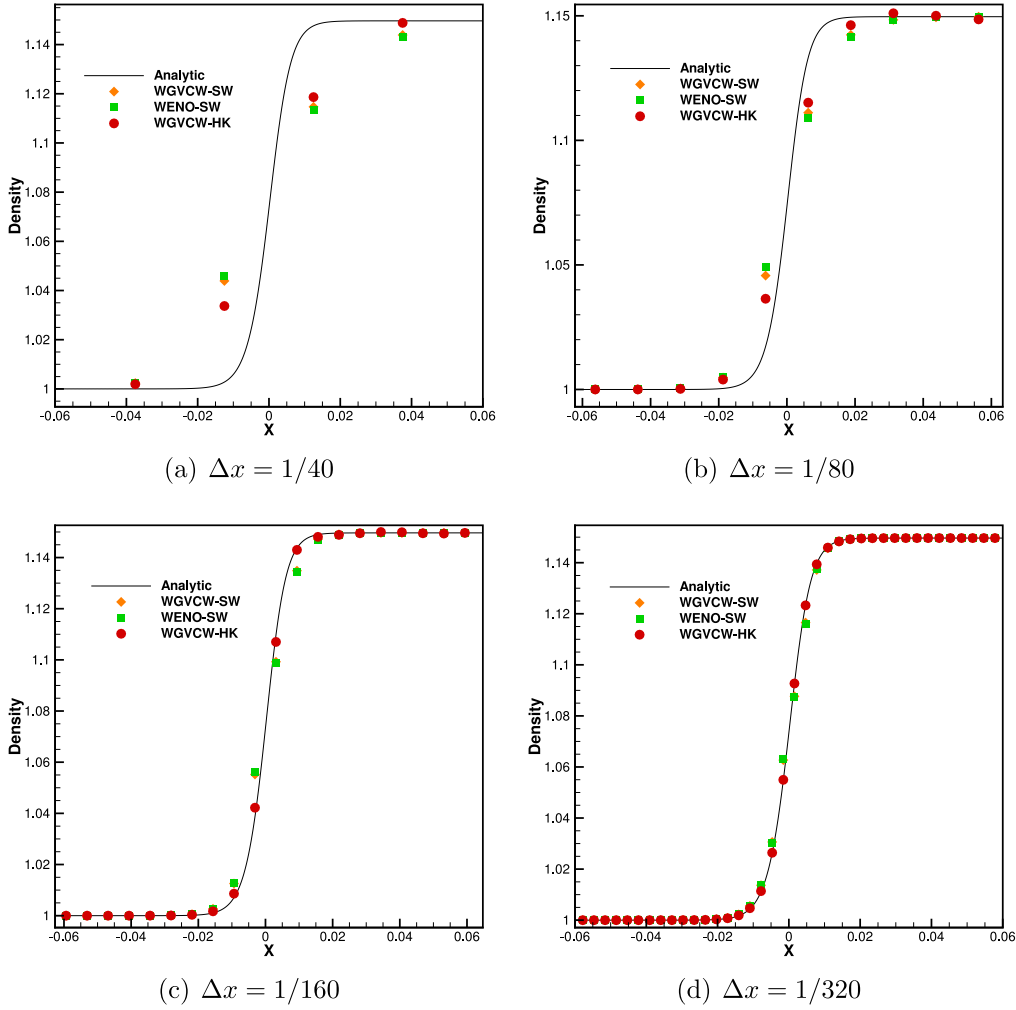


Fig. 9. Density profiles of Navier–Stokes shock structure problem with WGVCW–HK, WGVCW–SW, WENO–SW with 40 grid points (a), 80 grid points (b), 160 grid points (c), 320 grid points (d).

3.7. 2D Riemann problem

In this subsection, a classical two-dimensional Riemann problem [56] is resolved by the WGVCW–HK, WGVCW–KFVS, WGVCW–SW, and WENO–HK. The initial condition is:

$$(\rho, u, v, p) = \begin{cases} (1.0, 0.75, -0.5, 1.0), & 1.0 \leq x \leq 2.0, 1.0 \leq y \leq 2.0, \\ (2.0, 0.75, 0.5, 1.0), & 0.0 \leq x < 1.0, 1.0 \leq y \leq 2.0, \\ (1.0, -0.75, 0.5, 1.0), & 0.0 \leq x < 1.0, 0.0 \leq y < 1.0, \\ (3.0, -0.75, -0.5, 1.0), & 1.0 \leq x \leq 2.0, 0.0 \leq y < 1.0. \end{cases} \quad (46)$$

The computational domain is $[0, 2] \times [0, 2]$. The computational time is $t = 1.6$ s with 400×400 grid points. There are four slip lines in the solution of this case. The density contours are shown in Fig. 8. In which, it can be found that planar contact discontinuity interactions form four shear layers. In comparison with other schemes, WGVCW–HK presents more vortexes with the same grid points. It means that WGVCW–HK can capture the shear instabilities among four contact discontinuities with high resolution.

3.8. Navier–Stokes shock structure

In this subsection, the Navier–Stokes shock structure test [23], which is viscous, is considered. The WGVCW–HK, WGVCW–SW, and WENO–SW are applied to solve it. The initial condition is set as a stationary shock with $Ma = 1.1$, $\rho = 1$, $u = 1$, $\gamma = 5/3$. The constant

dynamic viscosity μ is set to be $\mu = 2.5 \times 10^{-4}$, and the Prandtl number Pr is 0.72 in this test. The analytic solution can be obtained by solving the ordinary differential equations [23]. The sixth-order central difference scheme in Section 2.4 is used to discrete the viscous term.

Fig. 9 are the computed density distributions based on different mesh sizes. It can be found that good mesh convergence has been achieved for every scheme. Moreover, WGVCW–HK performs overall better than other schemes, which indicates that WGVCW–HK is more accurate and less dissipative than others.

3.9. Laminar boundary layer

Another case of viscous flows is the laminar boundary layer problem. In this case, the fluid flows through a semi-infinite plate with a thickness of zero and forms the laminar boundary layer. There is an exact Blasius solution for the velocity distribution in the boundary layer. The grid number is 130×55 , where the x -direction coordinate 0 is the starting position of the plate, and the uniform free stream along the x -direction is in front of the plate. The minimum grid size in x -direction is 0.02, and the minimum grid size in y -direction is 0.02. The grid distribution is shown in Fig. 10. The Mach number is 0.2 and the Reynolds number is 1×10^5 , which is defined as $Re_\infty = U_\infty L/\nu$. The WGVCW–HK, WGVCW–SW and WENO–SW methods are used to deal with the convection terms, and the 6th order central difference scheme in Section 2.4 are used to deal with the viscous terms. Figs. 11–12 show the velocity distributions in x and y directions at $x = 20.44$. The η in

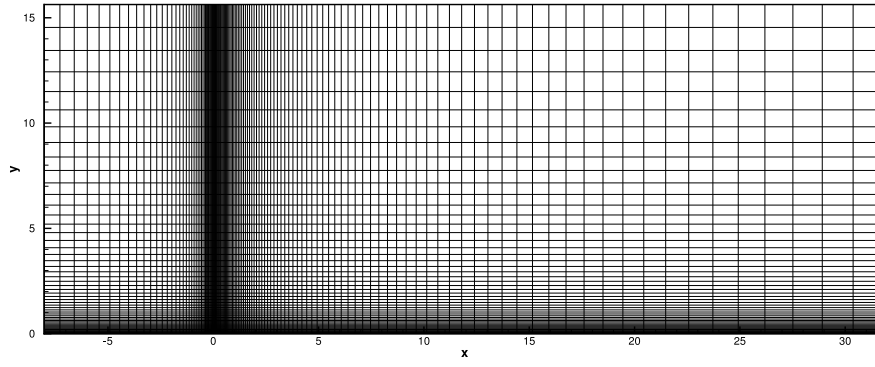


Fig. 10. Grid distribution of the laminar boundary layer problem.

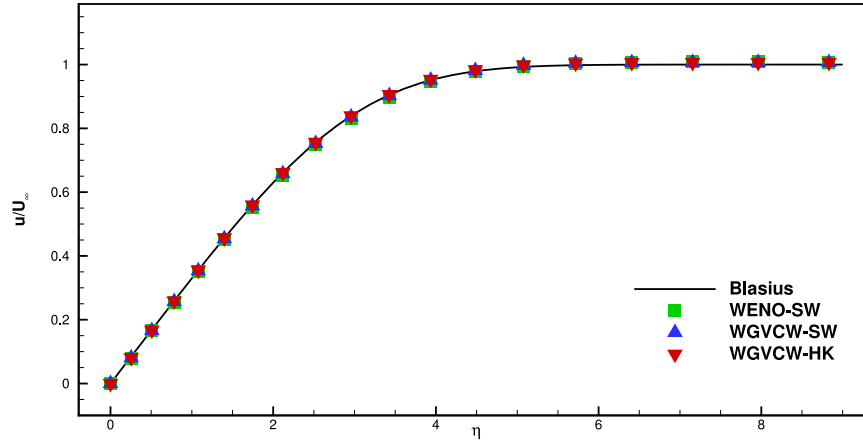


Fig. 11. U velocity distribution of the laminar boundary layer problem with WGVCW-HK, WGVCW-SW, WENO-SW at $x = 20.44$.

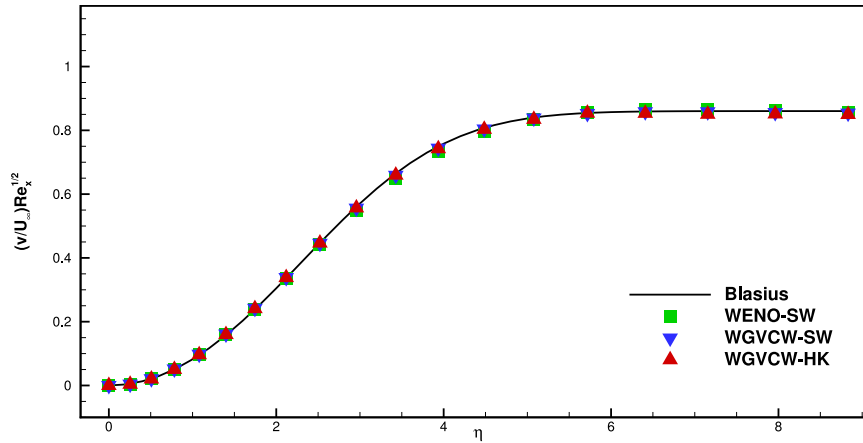


Fig. 12. V velocity distribution of the laminar boundary layer problem with WGVCW-HK, WGVCW-SW, WENO-SW at $x = 20.44$.

Figs. 11–12 is defined as $\eta = y\sqrt{U/(vx)}$. The distributions of velocity U and V calculated by the WGVCW-HK, WGVCW-SW and WENO-SW are very close, which agree well with the Blasius solution.

3.10. The computational cost

In this subsection, the computational cost of the hybrid kinetic WGVCW-WENO scheme is numerically investigated. The Shu–Osher problem in Section 3.3 and the double Mach reflection problem in Section 3.6 are taken as the test objects. The numerical tests are completed in the Windows system with single-core, and the CPU is Intel

i7-6700. Each test is repeated five times, and the calculation time given in Table 5 is the average of five tests.

As shown in Table 5, the CPU time for WGVCW-HK is 14% more than that for WGVCW-SW in Shu–Osher problem. In the double Mach reflection problem, the CPU time for WGVCW-HK is roughly 7% more than that for WGVCW-SW.

4. Conclusion

A high-order hybrid kinetic WGVCW-WENO scheme for compressible flow simulations is proposed in this paper. The new scheme inherits the hybrid kinetic method proposed by [50], which considers the effects

Table 5

The CPU time(in seconds) for WGVCW-HK, WGVCW-KFVS, WGVCW-SW with single-core in Shu–Osher problem and double Mach reflection problem.

Test case and efficiency	WGVCW-HK	WGVCW-KFVS	WGVCW-SW
Shu–Osher problem	1.44(1.14)	1.29(1.02)	1.26(1.00)
Double Mach reflection problem	3625.23(1.07)	3444.58(1.01)	3397.36(1.00)

of both the free transfer and the collision of gas molecules and is combined with the WGVC–WENO reconstruction technique in [45]. The new scheme has the characteristics: In smooth regions, the collision-related flux with small dissipation plays a leading role with the WGVC reconstruction technique. In the vicinity of discontinuous regions, the collisionless KFVS-type flux with large dissipation and WENO reconstruction technique are dominant.

Numerical experiments show that the new scheme is more accurate, less dissipative than [50] and other FVS methods, using the KFVS method and Steger–Warming method as examples. Several complex one-dimensional and two-dimensional examples show that the new scheme achieves not only high accuracy and low dissipation but also strong robustness and shock-capturing ability. Besides, the Titarev–Toro problem results show that the new scheme has a good capturing ability for high-frequency waves. In terms of the efficiency, the CPU time for WGVCW–HK is acceptable as shown in numerical examples.

CRediT authorship contribution statement

Kang He: Conceptualization, Methodology, Software, Writing – original draft. **Hongwei Liu:** Conceptualization, Supervision, Writing – review & editing. **Xinliang Li:** Methodology, Supervision, Writing – review & editing.

Declaration of competing interest

The authors declare that they have no known competing financial interests or personal relationships that could have appeared to influence the work reported in this paper.

Acknowledgments

This work was supported by the NSFC Projects (Nos.91852203, 11472278), National Key Research and Development Program of China (2019YFA-0405300, 2016YFA0401200), Strategic Priority Research Program of Chinese Academy of Sciences (Grant No. XDA17030100), and Science Challenge Project (TZ2016001). The authors thank the National Supercomputer Center in Tianjin (NSCC-TJ) and National Supercomputer Center in Guangzhou (NSCC-GZ) for providing computer time.

References

- [1] Harten A, Engquist B, Osher S, Chakravarthy SR. Uniformly high order accurate essentially non-oscillatory schemes, III. *J Comput Phys* 1987;71(1):231–303.
- [2] Liu XD, Osher S, Chan T. Weighted essentially non-oscillatory schemes. *J Comput Phys* 1994;115(1):200–12.
- [3] Jiang G-S, Shu C-W. Efficient implementation of weighted ENO schemes. *J Comput Phys* 1996;126(1):202–28.
- [4] Henrick AK, Aslam TD, Powers JM. Mapped weighted essentially non-oscillatory schemes: Achieving optimal order near critical points. *J Comput Phys* 2005;207(2):542–67.
- [5] Borges R, Carmona M, Costa B, Don WS. An improved weighted essentially non-oscillatory scheme for hyperbolic conservation laws. *J Comput Phys* 2008;227(6):3191–211.
- [6] Martin MP, Taylor EM, Wu M, Weirs VG. A bandwidth-optimized WENO scheme for the effective direct numerical simulation of compressible turbulence. *J Comput Phys* 2006;220(1):270–89.
- [7] Shen Y, Zha G. Improvement of weighted essentially non-oscillatory schemes near discontinuities. *Comput & Fluids* 2014;96:1–9.
- [8] Hong Z, Ye Z, Meng X. A mapping-function-free WENO-m scheme with low computational cost. *J Comput Phys* 2020;405:109145.
- [9] Suresh A, Huynh HT. Accurate monotonicity-preserving schemes with Runge–Kutta time stepping. *J Comput Phys* 1997;136(1):83–99.
- [10] Balsara DS, Shu CW. Monotonicity preserving weighted essentially non-oscillatory schemes with increasingly high order of accuracy. *J Comput Phys* 2000;160(2):405–52.
- [11] Dexun F, Yanwen M. Analysis of super compact finite difference method and application to simulation of vortex-shock interaction. *Internat J Numer Methods Fluids* 2001;36(7):773–805.
- [12] NA A, Shariff K. A high-resolution hybrid compact-ENO scheme for shock-turbulence interaction problems. *J Comput Phys* 1996;127(1):27–51.
- [13] Cockburn B, Shu C-W. The Runge–Kutta discontinuous Galerkin method for conservation laws V: multidimensional systems. *J Comput Phys* 1998;141(2):199–224.
- [14] Qiu J, Shu C-W. Runge–Kutta discontinuous Galerkin method using WENO limiters. *SIAM J Sci Comput* 2005;26(3):907–29.
- [15] Roe PL. Approximate Riemann solvers, parameter vectors, and difference schemes. *J Comput Phys* 1981;43(2):357–72.
- [16] Harten A, Leer LBV. On upstream differencing and godunov-type schemes for hyperbolic conservation laws. *Siam Rev* 1983;25(1):35–61.
- [17] Einfeldt B. On godunov-type methods for gas dynamics. *SIAM J Numer Anal* 1988;25(2):294–318.
- [18] Steger JL, Warming RF. Flux vector splitting of the inviscid gasdynamic equations with application to finite-difference methods. *J Comput Phys* 1981;40(2):263–93.
- [19] Leer BV. Flux-vector splitting for the Euler equations. In: International conference on numerical methods in fluid dynamics. 1982.
- [20] Mandal J, Deshpande S. Kinetic flux vector splitting for Euler equations. *Comput Fluids* 1994;23(2):447–78.
- [21] Xu K, Prendergast KH. Numerical Navier–Stokes solutions from gas kinetic theory. *J Comput Phys* 1994;114(1):9–17.
- [22] Xu K. Gas-kinetic schemes for unsteady compressible flow simulations. In *Computational fluid dynamics, annual lecture series, 29 th, Rhode-Saint-Genese, Belgium*, 1998.
- [23] Xu K. A gas-kinetic BGK scheme for the Navier–Stokes equations and its connection with artificial dissipation and Godunov method. *J Comput Phys* 2001;171(1):289–335.
- [24] Deshpande S. Kinetic theory based new upwind methods for inviscid compressible flows. In: 24th aerospace sciences meeting. 1986. p. 275.
- [25] Pullin D. Direct simulation methods for compressible inviscid ideal-gas flow. *J Comput Phys* 1980;34(2):231–44.
- [26] Chou S-Y, Baganoff D. Kinetic flux–vector splitting for the Navier–Stokes equations. *J Comput Phys* 1997;130(2):217–30.
- [27] Chen Y, Jiang S. Modified kinetic flux vector splitting schemes for compressible flows. *J Comput Phys* 2009;228(10):3582–604.
- [28] Li Q, Xu K, Fu S. A high-order gas-kinetic Navier–Stokes flow solver. *J Comput Phys* 2010;229(19):6715–31.
- [29] Luo J, Xu K. A high-order multidimensional gas-kinetic scheme for hydrodynamic equations. *Sci China Technol Sci* 2013;56(10):2370–84.
- [30] Pan L, Xu K, Li Q, Li J. An efficient and accurate two-stage fourth-order gas-kinetic scheme for the Euler and Navier–Stokes equations. *J Comput Phys* 2016;326:197–221.
- [31] Pan L, Cheng J, Wang S, Xu K. A two-stage fourth-order gas-kinetic scheme for compressible multicomponent flows. *Commun Comput Phys* 2017;22(4):1123–49.
- [32] Pan L, Xu K. Two-stage fourth-order gas-kinetic scheme for three-dimensional Euler and Navier–Stokes solutions. *Int J Comput Fluid Dyn* 2018;32(10):395–411.
- [33] Ji X, Pan L, Shyy W, Xu K. A compact fourth-order gas-kinetic scheme for the Euler and Navier–Stokes equations. *J Comput Phys* 2018;372:446–72.
- [34] Ji X, Zhao F, Shyy W, Xu K. A hwen reconstruction based high-order compact gas-kinetic scheme on unstructured mesh. *J Comput Phys* 2020;410:109367.
- [35] Zhao F, Ji X, Shyy W, Xu K. An acoustic and shock wave capturing compact high-order gas-kinetic scheme with spectral-like resolution. *Int J Comput Fluid Dyn* 2020;34(10):731–56.
- [36] Pan L, Xu K. An arbitrary-Lagrangian-Eulerian high-order gas-kinetic scheme for three-dimensional computations. *J Sci Comput* 2021;88(1):1–29.
- [37] Pan L, Cao G, Xu K. Fourth-order gas-kinetic scheme for turbulence simulation with multi-dimensional WENO reconstruction. *Comput Fluids* 2021;221:104927.
- [38] Ji X, Zhao F, Shyy W, Xu K. A family of high-order gas-kinetic schemes and its comparison with Riemann solver based high-order methods. *J Comput Phys* 2018;356:150–73.
- [39] Cao G, Pan L, Xu K. Three dimensional high-order gas-kinetic scheme for supersonic isotropic turbulence i: criterion for direct numerical simulation. *Comput Fluids* 2019;192:104273.
- [40] Zhu Y, Zhong C, Xu K. Gks and ugks for high-speed flows. *Aerospace* 2021;8(5):141.
- [41] NA A, Shariff K. A high-resolution hybrid compact-ENO scheme for shock-turbulence interaction problems. *J Comput Phys* 1996;127(1):27–51.
- [42] Pirozzoli S. Conservative hybrid compact-WENO schemes for shock-turbulence interaction. *J Comput Phys* 2002;178(1):81–117.

- [43] Ren YX, Liu M, Zhang H. A characteristic-wise hybrid compact-WENO scheme for solving hyperbolic conservation laws. *J Comput Phys* 2003;192(2):365–86.
- [44] Sun ZS, Ren YX, Larricq C, Zhang SY, Yang YC. A class of finite difference schemes with low dispersion and controllable dissipation for DNS of compressible turbulence. *J Comput Phys* 2011;230(12):4616–35.
- [45] He Z, Li X, Liang X. Nonlinear spectral-like schemes for hybrid schemes. *Sci China Phys Mech Astron* 2014;57(4):753–63.
- [46] Zhao Z, Chen Y, Qiu J. A hybrid Hermite WENO scheme for hyperbolic conservation laws. *J Comput Phys* 2020;405:109175.
- [47] Krivodonova L, Xin J, Remacle JF, Chevaugeon N, Flaherty JE. Shock detection and limiting with discontinuous Galerkin methods for hyperbolic conservation laws. *Appl Numer Math* 2004;48(3):323–38.
- [48] Li G, Qiu J. Hybrid weighted essentially non-oscillatory schemes with different indicators. *J Comput Phys* 2010;229(21):8105–29.
- [49] Lv Y, See YC, Ihme M. An entropy-residual shock detector for solving conservation laws using high-order discontinuous Galerkin methods. *J Comput Phys* 2016;322:448–72.
- [50] Liu H. A hybrid kinetic WENO scheme for inviscid and viscous flows. *Internat J Numer Methods Fluids* 2015;79(6):290–305.
- [51] Shu C-W, Osher S. Efficient implementation of essentially non-oscillatory shock-capturing schemes. *J Comput Phys* 1988;77(2):439–71.
- [52] Fu D, Ma Y, Kobayashi T, et al. Nonphysical oscillations in numerical solutions: reason and improvement. *CFD J* 1996;4(4):427–50.
- [53] Titarev VA, Toro EF. Finite-volume WENO schemes for three-dimensional conservation laws. *J Comput Phys* 2004;201(1):238–60.
- [54] Liao F, He G. High-order adapter schemes for cell-centered finite difference method. *J Comput Phys* 2020;403:109090.
- [55] Woodward P, Colella P. The numerical simulation of two-dimensional fluid flow with strong shocks. *J Comput Phys* 1984;54(1):115–73.
- [56] Schulz-Rinne CW, Collins JP, Glaz HM. Numerical solution of the Riemann problem for two-dimensional gas dynamics. *SIAM J Sci Comput* 1993;14(6):1394–414.